Microstructural evolution in a precipitate-hardened (Fe_{0.3}Ni_{0.3}Mn_{0.3}Cr_{0.1})₉₄Ti₂Al₄ high entropy alloy during high-pressure torsion

Matthew Luebbe¹, Jiaqi Duan^{1,2}, Peipei Cao³, Zhaoping Lu³, Rinat K. Islamgaliev⁴, Ruslan Z. Valiev⁴, Yuzi Liu⁵, Haiming Wen^{1,*}

Abstract

High entropy alloys (HEAs) demonstrate high strength, thermal stability, and irradiation resistance, making them excellent candidate materials for applications in nuclear reactors and other harsh environments. Some studies have examined the use of high-pressure torsion (HPT) to strengthen HEAs through grain size reduction and strain hardening. However, no studies have investigated the effect of HPT on secondary phases (precipitates) within an HEA. Two alloys, (Fe_{0.3}Ni_{0.3}Mn_{0.3}Cr_{0.1})₉₄Ti₂Al₄ containing Ni(Ti, Al) B2 phase, and CrFe σ phase, and single-phase Fe_{0.3}Ni_{0.3}Mn_{0.3}Cr_{0.1}, were fabricated by casting and heat treatment. Both alloys were then processed with HPT to study microstructural evolution. Scanning electron microscopy (SEM) and transmission electron microscopy (TEM) were used to characterize the alloys before and after HPT processing. HPT processing produced a nanocrystalline structure in both alloys, but (Fe_{0.3}Ni_{0.3}Mn_{0.3}Cr_{0.1})₉₄Ti₂Al₄ exhibited a significantly smaller grain size and higher dislocation density than Fe_{0.3}Ni_{0.3}Mn_{0.3}Cr_{0.1}, with corresponding higher hardness. Before HPT, the (Fe_{0.3}Ni_{0.3}Mn_{0.3}Cr_{0.1})₉₄Ti₂Al₄ alloy consisted of large grain (~400 μm) and precipitates, including B2 of \sim 38 µm, B2 of \sim 0.7 µm average size, and small amounts of σ of \sim 1.5 µm average size. After HPT, the larger B2 precipitates were decreased in size and volume fraction, while the smaller B2 precipitates were completely dissolved; the σ precipitates appeared unaffected by HPT, likely due to their much higher hardness. Observation of the B2 precipitate distribution along radial distance indicates that the strain caused the precipitates to fracture at intermediate strain (γ =125) and dissolve at high strain (γ =280).

1. Introduction

High entropy alloys (HEAs) are a new class of alloys with multiple principal elements. They are typically defined as alloys with five or more elements with a content between 5 and 35 at% for each element [1-2]. This compositional complexity leads to severe lattice distortion, sluggish diffusion kinetics, and a high mixing entropy [3]. HEAs have been shown in the literature to possess unique properties, such as high strength, good thermal stability, good ductility, and

¹Department of Materials Science and Engineering, Missouri University of Science and Technology, Rolla, MO 65409, USA

²Warwick Manufacturing Group, University of Warwick, Coventry, CV4 7AL, UK

³State Key Laboratory for Advanced Metals and Materials, University of Science and Technology Beijing, Beijing 100083, China

⁴Institute of Physics of Advanced Materials, Ufa University of Science and Technologies, Ufa 450076, Russia

⁵Center for Nanoscale Materials, Argonne National Laboratory, Lemont, IL 60439, USA

^{*}Corresponding author: wenha@mst.edu (H.M. Wen)

excellent oxidation and irradiation resistance [4-12]. Most HEA studies are focused on single-phase structures [13-15], but some studies have also explored precipitation strengthening and intermetallic formation in HEAs [16-18]. For example, He et al. [16] developed a (FeNiCoCr) $_{94}$ Ti $_{2}$ Al $_{4}$ alloy with nanoscale γ ' precipitates after aging, which exhibited a yield strength of 1005 MPa and an ultimate tensile strength of 1273 MPa, with a tensile ductility of 17%. The precipitates provide HEAs with excellent strength as well as thermal stability and irradiation resistance [19-21].

High-pressure torsion (HPT) is a severe plastic deformation method that involves pressing a thin disc between two rotating anvils. This method produces significant grain refinement, typically resulting in a nanocrystalline structure and high dislocation density, often on the order of 10¹⁵ m⁻² [22-23]. HPT on conventional alloys such as steels has produced impressive strengths [24-26]. For example, Scheriau et al. [25] subjected 316L stainless steel disks to 4 turns of HPT under 6 GPa stress at room temperature, which caused the microhardness to increase from 160 HV to almost 500 HV. HPT has been performed on HEAs to produce similar results [27-30]. Some studies focused on grain refinement and other strengthening mechanisms under HPT in HEAs [31-33]. For instance, several studies, including the one by Yu et al [31], have shown the formation of deformation twinning after HPT processing, contributing to the high dislocation density. Schuh et al. [32] also observed a bimodal grain size distribution in HPT processed CoCrFeMnNi HEA, which yielded a good combination of strength and ductility.

HPT has also been indicated to affect precipitates and second phases in conventional alloys, including Cu and Al alloys [34-36]. The large strain produced by the HPT processing can alter the local solubility, causing some precipitates to dissolve and others to form. For example, Mg alloys have been shown, by Meng et al [37], to form precipitates during HPT even at room temperature, and some studies have used this to achieve better grain refinement [37-38]. On the other hand, Cu alloys with pre-existing precipitates sometimes experience precipitate dissolution under HPT [39-40]. Specifically, Straumal et al. [40] studied a Cu-3.9% Ag alloy, which experienced dissolution and re-precipitation of Ag precipitates after 5 turns of HPT under 6 GPa at room temperature. Such precipitate formation/dissolution phenomena during HPT have not been well studied in HEAs, with only a few studies on phase changes due to HPT [41-43]. One of these studies was on the AlCrFe₂Ni₂ alloy, whose B2/BCC/FCC structure changed to FCC after 1 turn of HPT under 6 GPa temperature [41]. In this current study, $Fe_{0.3}Ni_{0.3}Mn_{0.3}Cr_{0.1}$ (Fe_{0.3}Ni_{0.3}Mn_{0.3}Cr_{0.1})₉₄Ti₂Al₄ alloys were subjected to HPT, with the former being a single-phase alloy previously studied [44] and the latter with Ti and Al added to produce precipitates. HPT processing can serve to further strengthen the alloys but could interfere with the precipitation strengthening already present in (Fe_{0.3}Ni_{0.3}Mn_{0.3}Cr_{0.1})₉₄Ti₂Al₄. Thus, the effects of HPT on grain refinement and precipitate evolution were investigated.

2. Experimental Procedures

Bulk Fe_{0.3}Ni_{0.3}Mn_{0.3}Cr_{0.1} and (Fe_{0.3}Ni_{0.3}Mn_{0.3}Cr_{0.1})₉₄Ti₂Al₄ alloys (referred to as FeNiMnCr and FeNiMnCrTiAl, respectively, hereafter in this paper) were cast using arc-melting from pure elements. The purity of each element was 99.995%, 99.995%, 99.99%, 99.99%, 99.99% for Fe, Ni, Mn, Cr, Ti, and Al, respectively. After casting, to ensure compositional homogeneity,

both alloys were homogenized at 1200 °C for 10 hours. To introduce precipitates in the FeNiMnCrTiAl alloy, it was cold rolled to 30% reduction, solution treated at 1000 °C for 2 hours, and then aged at 800 °C for 18 hours. After heat treatment, both alloys were processed via HPT at 200 °C under a pressure of 6 GPa for 10 turns at a rotation speed of 0.2 turns per minute. After HPT processing, the diameter of the samples is ~10 mm, with a final thickness of ~1 mm.

Samples from before and after HPT processing were characterized with scanning electron microscopy (SEM) and transmission electron microscopy (TEM). SEM was performed using an FEI Helios Dual-Beam Nanolab at 20 kV. TEM specimens were lifted out using focused ion beam on the Helios and characterized on an FEI F20 TEM at 200 kV. TEM specimens from the HPT samples were taken in a radial direction of ~4 mm distance from the center. Further TEM of the FeNiMnCrTiAl alloy after HPT processing was performed on a JEOL JEM 2100F and FEI Talos F200X, both operating at 200 kV. Microhardness measurements were performed using a Struers Duramin 5 Vickers hardness tester, with a force and time of 4.9 N and 10 s, on the HPT discs at varying distances from the center to the edge of the disc.

Strengthening analysis was performed to determine the contributions from grain size, dislocation density, and precipitates to the strength. X-ray diffraction (XRD) was used to determine the dislocation density using peak broadening and the Williamson-Hall method. XRD was carried out using a Philips MRD diffractometer, with diffraction angles ranging from 0 to 130° and a scan time of 30 min.

3. Results

3.1 Coarse-grained microstructures before HPT

The samples after heat treatment were characterized using SEM and TEM, combined with energy-dispersive X-ray spectroscopy (EDS) to determine the grain structures and distributions of the elements prior to HPT processing. Both samples showed coarse grains (up to hundreds of microns), with the FeNiMnCr (Fig. 1) having larger grains (grain boundary marked in Fig. 1a) than FeNiMnCrTiAl (Fig. 2). FeNiMnCr was elementally homogeneous with no segregation on grain boundaries. It exhibited some Mn inclusions, which have been reported previously for this composition [44]. FeNiMnCrTiAl showed patches rich in Mn, Ni, Ti, and Al (which were B2 precipitates) within grains; meanwhile, those elements were also segregated to the grain boundaries, with 45% Ni, 7% Ti and 7% Al at the boundaries. These B2 precipitates in the grains were ~38 μm in size and made up ~6.7% of the microstructure.

To verify the identity of the B2 precipitates, TEM was performed on CG FeNiMnCrTiAl. TEM results displayed in Figure 3 indicate that in addition to the B2 precipitates (Fig. 3d), there is also a CrFe rich phase in the sample. This phase is confirmed to be σ phase in Figure 3e, with an average size of $\sim 1.5~\mu m$. Figure 4 shows several significantly smaller elongated precipitates within the FCC grains, $\sim 1~\mu m$ long on average with an area equivalent diameter of $\sim 0.7~\mu m$. From EDS, these precipitates were enriched in Ni and Al, depleted in Fe and Cr, with significant amounts of Mn and Ti (Table 1); they exhibited a BCC/B2 structure as determined by selected-area electron diffraction (SAED) pattern (indexed in Figure 4c). These results indicate that the smaller

precipitates were also B2 [45, 46], and both B2 and σ precipitate phases existed in FeNiMnCrTiAl after aging at 800 °C, before HPT

Table 1: Composition and size of B2 precipitates before HPT in FeNiMnCrTiAl. Compositions are in at.%, measured using SEM-EDS for the large B2 and TEM-EDS for the small B2 precipitates. Area equivalent diameter was used to approximate size.

	Diameter (μm)	Number Density (/m²)	Area Fraction	Fe	Ni	Mn	Cr	Ti	Al
Large B2	37.78	5.95×10^7	6.67%	16.88	35.53	31.16	6.20	4.23	6.00
Small B2	0.703	3.53×10^{11}	13.74%	4.47	55.30	20.00	0.82	3.44	15.97

3.2 Grain structure and hardness after HPT

Figure 5 shows the grain structures for FeNiMnCr and FeNiMnCrTiAl after HPT processing. The grains are elongated along the shearing direction, which is marked on the images, and the average length, width, and aspect ratio of the grains are given in Table 2. Clearly, the grains in FeNiMnCrTiAl remain smaller after HPT processing. The aspect ratio of the grains in both samples is very similar. The nanocrystalline structure observed in Figure 5 demonstrates that significant grain refinement has been achieved by HPT. The hardness of the HPT discs as a function of radius from the center is presented in Figure 6. The hardness increased slightly from the center to the edge, likely due to increased strain and grain refinement. Also, FeNiMnCrTiAl exhibited hardness up to 70 HV higher than that of FeNiMnCr. The detailed reasoning behind this effect will be elucidated in the discussion section.

Table 2: Average grain sizes and aspect ratios with standard deviation in HPT processed HEAs

Alloy	Length (nm)	Width (nm)	Aspect ratio
FeNiMnCr	130 ± 79	37 ± 14	3.50 ± 1.57
FeNiMnCrTiAl	85 ± 46	27 ± 9	3.24 ± 1.52

3.3 HPT effect on secondary phases (precipitates)

In addition to the decreased grain size, the HPT processing also affected the secondary phases (precipitates) present in FeNiMnCrTiAl. Figure 7 displays an example of the retained phases after HPT, taken near the edge of the disc. Scattered areas of NiTiAl enrichment can be found, \sim 3 µm in diameter. As it is unlikely that the small pre-existing B2 precipitates grew at 200 °C in less than 1 hour during HPT processing, this suggests that the larger pre-existing B2 precipitates have been refined into much smaller ones. Cr enriched spots are also observed in Figure 7, which are likely retained σ . These σ phase particles are relatively unaffected by HPT processing, with an average size of \sim 1.4 µm after HPT. In addition, the overall phase fraction of the B2 has decreased and the number density has risen compared to the pre-HPT state, as quantified in Figure 8 (2×109/m²) compared to Table 1 (6×107/m²). Figure 8 presents the statistics of the B2

precipitates from SEM image analysis within the HPT disc. The observed trend is that size and phase fraction drop from center to edge, while the number density rises and then drops. No smaller (submicron to nanometer scale) B2 precipitates were observed under TEM, indicating that the 0.7 µm B2 precipitates present before HPT dissolved rather than being refined, and the larger (38 µm) B2 regions were refined. This is supported by the literature as elucidated in the discussion section. Figure 9 shows that the areas of NiTiAl enrichment are elongated along the shearing direction in which the grains are elongated. Analysis of the diffraction patterns on such areas suggest an BCC structure, which indicates that they are B2 given the NiTiAl enrichment observed under STEM-EDS. As the TEM sample was taken directly from one of the NiTiAl enriched areas visible in Figure 7, this confirms that the NiTiAl enriched areas retained after HPT are B2.

4. Discussion

4.1 Grain refinement via HPT in different alloys

As noted previously in Table 2 and later in Figure 10, the grain size and dislocation density differ between the FeNiMnCr and FeNiMnCrTiAl alloys despite being subjected to the same HPT processing conditions. There could be several different explanations for this. Several papers have reported grain refinement saturation due to HPT or other severe plastic deformation techniques [49, 50]. A paper by Mohamed and Dheda [51] attempted to model the minimum grain size achieved by HPT in a given alloy. According to the model, the minimum grain size can be affected by the melting temperature and bulk modulus of the alloy, both of which primarily rely on composition, and not processing or microstructure. However, more recent studies have questioned the assertion that initial processing does not affect grain refinement by HPT. Sabbaghianrad et al. [52] tested Al and Mg alloys under sole HPT as well as HPT following equal channel angular pressing (ECAP) and found that the additional grain refinement from pre-HPT processing (ECAP in that study) resulted in smaller final grain sizes. They also observed that presence of precipitates could facilitate grain refinement while fragmentation of precipitates could reduce grain refinement. Fundamentally, the grain refinement occurs by accumulation of dislocations and their rearrangement into cell or grain boundaries, followed by transformation of low-angle to high-angle boundaries. Thus, grain refinement is counteracted by recovery. Precipitates can hinder recovery (until they are fragmented) and therefore facilitate dislocation accumulation/rearrangement, promoting grain refinement. The HPT processing temperature in this study is too low for dynamic recrystallization and therefore that does not need to be considered [53, 54]. In summary, it seems likely that the presence of B2 and σ precipitates and slightly smaller initial grain size in FeNiMnCrTiAl as compared to FeNiMnCr contributed to the differences between the two alloys in grain size and dislocation density after HPT.

4.2 Effects of HPT on precipitates

Before HPT, the FeNiMnCrTiAl alloy possessed two types of precipitates (Figure 2): large precipitates \sim 38 μ m in diameter, and small elongated precipitates \sim 0.7 μ m in diameter. The chemistry and morphology of both appear to be similar to those of B2 [46], and both are confirmed as such (Figures 3 and 4). The NiTiAl precipitates after HPT are also confirmed to be B2 (Figure 9). Also, CrFe-rich σ rich precipitates \sim 1.5 μ m average size existed in the FeNiMnCrTiAl alloy

before HPT. These σ phase precipitates remain almost unchanged after HPT (Figure 7), though not in very high quantities (0.27% by area). The difference in behavior between σ and B2 during HPT is likely due to the immense difference in hardness between the two, with σ having a hardness of 1076 HV (3515 MPa) [55] and B2 possessing a hardness of 330 HV (1078 MPa) [56]. After HPT, the remaining B2 precipitates exhibit variation in precipitate statistics along the radial directions. For HPT processed discs, the imposed strain also increases with distance from the center as estimated by Equation (1) [57]:

$$\gamma = \frac{2\pi NR}{h} \tag{1}$$

where N is the number of turns, R is the distance from the center, and h is the initial thickness (1 mm). Given this equation and the precipitate statistics, the likely reasons behind the changes to precipitates during HPT processing can be discussed. From low to intermediate strains (center to 2 mm, or strains of 12-125), the precipitate size decreases, but the number density increases, and the area fraction decreases more slowly than the size. This indicates that at intermediate strain levels, the strain is enough to break the B2 precipitates, but not enough to dissolve them. Precipitate fragmentation such as this was mentioned in several papers [57-59]. For example, Korneva et al [58] reported fragmentation of Ag precipitates before dissolution and Ivanisenko et al [57] observed similar behavior for cementite in steels. From intermediate to high strains (2 mm to edge, or 125-280), the size, number density, and area fraction of the precipitates all decrease, indicating that the strain levels are high enough to get the some of the B2 precipitates to dissolve into the matrix, though a strain of 280 from 10 turns of HPT at 6 GPa was not enough to get them all to dissolve. Some mechanisms for this partial dissolution will be discussed. Ivanisenko et al [57] mentioned that severe plastic deformation can increase interfacial energy due to dislocation buildup, effectively increasing the critical size of the precipitates that can be dissolved, as explained by Languillaume et al [60]. Korneva et al [58] showed dissolution of Ag precipitates, and an increase in Ag solubility in Cu by HPT processing. This combination of increased interfacial energy and enhanced solubility due to strain promotes dissolution of smaller, fragmented precipitates. However, significant diffusion rate is needed to realize the dissolution. 200 °C (the HPT processing temperature) is relatively low to bring significant diffusion. However, Beach et al [59] suggested that shear strain can reduce the energy barrier for diffusion, and Jacob et al [61] maintained that the increased dislocation and grain boundary density can serve as pipe diffusion sites. Both factors serve to increase the diffusion rate, allowing the precipitates to dissolve. Also worth mentioning is that in Ivanisenko et al [57], a strain of 300 was sufficient to completely dissolve cementite, but a strain of 280 was not sufficient to completely dissolve the B2 in this alloy.

The effect of temperature on the dissolution or precipitation of secondary phases also warrants discussion. This study used a slightly elevated temperature of 200 °C instead of room temperature for HPT processing. Depending on the alloy, room temperature HPT can lead to dissolution of pre-existing precipitates [38, 58] or new precipitation [34, 36]. Studies at different temperature can help determine temperature effects. Beach et al [59] showed fracture and dissolution of Nb precipitates in Cu-Nb alloys at -78 °C, suggesting that very low temperatures facilitate dissolution rather than precipitation. Zhang et al [34], on the other hand, directly

compared room temperature and 200 °C HPT for Al-7075 alloy. After 5 turns at both temperatures, hexagonal η phases were shown to form. However, at room temperature, the increase to 10 turns caused the precipitates to disappear, while the precipitates increased at 200 °C after 10 turns. This indicates that while temperature has some effect on whether precipitation or dissolution will occur, shear strain is the deciding factor. This argument is supported by Straumal et al [39, 40], who reported that shear strain essentially produces an effect on diffusion similar to that by an effective annealing temperature, $T_{\rm eff}$, which is significantly higher than the actual HPT processing temperature.

4.3 Strengthening Analysis

The acquired SEM and TEM images were analyzed to determine the grain size and precipitate statistics (Table 2, Figure 8). XRD data were collected from HPT processed FeNiMnCr and FeNiMnCrTiAl and analyzed to estimate the dislocation density (Figure 10). The XRD peaks for FeNiMnCrTiAl in Figure 10 correspond only to the FCC matrix phase, as the B2 phase was not present in large enough quantities to show up under XRD. Williamson-Hall plots for each material are included as insets and will be used to determine dislocation density later in this section.

The results from the microstructural analyses were used as input to determine the strengthening from each strengthening mechanism in the HPT processed samples. The dislocation density is estimated from the XRD data using a Williamson Hall plot, with the equation of the line given by Equation 2 [16]:

$$\beta cos\theta = \frac{\kappa\lambda}{D} + (4sin\theta) * \varepsilon \tag{2}$$

where β is the peak broadening from the XRD data, K=0.9, λ =1.5405 Å is the Cu K α wavelength used for XRD, D is the crystallite size (not grain size), and ϵ is the lattice strain, which is the slope of the W-H plot. The plots are shown in Figure 10. From these graphs the values of ϵ and D can be determined as 2.46×10^{-3} and 25.9 nm respectively for FeNiMnCr, and 2.34×10^{-3} and 19.9 nm respectively for FeNiMnCrTiAl. Equation 3 converts lattice strain to dislocation density [16]:

$$\rho = 2\sqrt{3} * \frac{\varepsilon}{Db} \tag{3}$$

where b is the Burger's vector, which is 0.256 nm for FeNiMnCr and 0.257 nm for FeNiMnCrTiAl. This gives a dislocation density of 1.28×10^{15} /m² for FeNiMnCr and 1.58×10^{15} /m² for FeNiMnCrTiAl. Given this information, the dislocation strengthening is calculated with Equation $4 \cdot$

$$\Delta \sigma_D = M\alpha G b \rho^{1/2} \tag{4}$$

where G is the shear modulus, 78.5 GPa [16], M=3.06, and α =0.2. The dislocation strengthening is 439 MPa for FeNiMnCr and 488 MPa for FeNiMnCrTiAl.

The grain boundary strengthening (i.e., grain size effect on strength) is included in the Hall-Petch relationship in Equation 5 [16]:

$$\sigma_{y} = \sigma_{0} + \frac{\kappa}{\sqrt{d}} \tag{5}$$

where σ_y is the yield strength, σ_0 is the lattice friction stress, K is the Hall-Petch coefficient, and d is the grain size determined from TEM. Given the elongated grains in both samples, the grain size used is the area-equivalent circle diameter, which is 77.6 nm for FeNiMnCr and 53.3 nm for FeNiMnCrTiAl. The σ_0 for these alloys is given later, but the grain boundary strengthening itself can be calculated without σ_0 using Equation 6:

$$\Delta \sigma_G = \frac{\kappa}{\sqrt{d}} \tag{6}$$

Using the Hall-Petch coefficient for the FeCoNiMnCr system in Liu et al [47], 226 MPa μ m^{1/2}, the grain boundary strengthening for each alloy is calculated as 628 MPa for FeNiMnCr and 777 MPa for FeNiMnCrTiAl.

For the FeNiMnCrTiAl alloy, changes in the B2 precipitate characteristics were observed after HPT processing, with the statistics displayed in Figure 8. Given the size of the B2 precipitates, Orowan looping is likely the dominant mechanism of precipitation strengthening, which is calculated using Equation 7 [48]:

$$\Delta\sigma_{or} = M \frac{0.4Gb}{\pi\lambda} \frac{\ln(2\bar{r}/b)}{\sqrt{1-\nu}} \tag{7}$$

where $\bar{r} = \sqrt{\frac{2}{3}}r = 1.515 \,\mu m$ is the mean radius of circular cross-section through a spherical B2 precipitate, v is the Poisson's ratio for the alloy, 0.31 [16], and λ is the inter-precipitate edge-to-edge spacing, given by Equation 8.

$$\lambda = 2\bar{r} \left(\sqrt{\frac{\pi}{4f}} - 1 \right) = 11.60 \ \mu m \tag{8}$$

Given these equations, the strengthening from precipitates ranges from 5.32 MPa on the edge of HPT disc to 7.65 MPa for 2 mm from the center. In addition, given the average radius of the σ of 689 nm and their area fraction of 0.27%, the strengthening from σ precipitates can be estimated as 4.39 MPa, making the total strengthening from precipitates 12.04 MPa.

For HEAs, solid solution strengthening can be a major source of strengthening, but the alloy complexity is too great for traditional models to work. For this study, however, the two alloys are similar in composition except for Ti and Al additions, and thus Equation 9 can be used to link their solid solution strengthening components [16]:

$$\Delta \sigma_S = M \frac{G * \varepsilon_S^{3/2} * c^{1/2}}{700} \tag{9}$$

where c is the atomic concentration of the Ti and Al solutes, 0.06, and ε_s is the interaction parameter, which is given by Equation 10.

$$\varepsilon_S = \left| \frac{\varepsilon_G}{1 + 0.5\varepsilon_G} - 3 * \varepsilon_a \right| \tag{10}$$

where ε_G is the elastic mismatch and ε_a is the atomic size mismatch. The elastic mismatch is typically negligible compared to the atomic size mismatch, which is given as Equation 11:

$$\varepsilon_a = \frac{1}{a} \frac{\partial a}{\partial c} = 0.0633 \tag{11}$$

Assuming the Ti and Al are totally dissolved into the matrix, the maximum solid solution strengthening from the Ti and Al additions is 6.95 MPa.

Considering the literature data for $Fe_{0.3}Ni_{0.3}Mn_{0.3}Cr_{0.1}$, 507 MPa is used as σ_0 for both alloys [44]. This value contains solid solution strengthening, but the additional solid solution strengthening from Ti and Al addition is 7 MPa for FeNiMnCrTiAl, based on the previous equations. A graphical representation of strengthening contributions from different strengthening mechanisms for both FeNiMnCr and FeNiMnCrTiAl is displayed in Figure 11. The calculated yield strengths of FeNiMnCr and FeNiMnCrTiAl are 1574 MPa and 1787 MPa, respectively. Using empirical relationship between Vickers hardness and strength (where strength is approximately 1/3 of hardness in MPa), the experimentally measured Vickers hardness of FeNiMnCr (469 HV) and FeNiMnCrTiAl (540 HV) is converted to strength of 1532 MPa (=469 × 9.8÷3) and 1764 MPa (=540 × 9.8÷3), respectively. The calculated strength values are slightly higher than the experimental values, however, the two are very close to each other.

5. Conclusions

Two high-entropy alloys, a single phase Fe_{0.3}Ni_{0.3}Mn_{0.3}Cr_{0.1} and a precipitation-hardened (Fe_{0.3}Ni_{0.3}Mn_{0.3}Cr_{0.1})₉₄Ti₂Al₄ were fabricated via casting and heat treatment. These alloys were then processed via 10 turns of HPT under 6 GPa at 200°C. Microstructural characterization revealed the extent of grain size reduction, as well as the effect of HPT processing on the precipitates present in FeNiMnCrTiAl. The main conclusions of the study are:

- 1) Before HPT processing, both alloys had large grains of hundreds of microns. The FeNiMnCrTiAl alloy possessed small (~0.7 μm average diameter) and large (~38 μm average diameter) B2 precipitates inside grains, as well as NiTiAl solute segregations on grain boundaries and small (~1.5 μm average diameter) σ precipitates inside grains.
- 2) After HPT processing, the grain size was reduced to tens of nanometers, with the grains elongated along the shearing direction. The large B2 precipitates have also decreased in size to $\sim 3~\mu m$ and in area fraction, making up less than 1% of the area at highest strain, compared to 6.7% before HPT. The variations across the radius of the disc suggests the strain from HPT caused precipitates to break apart and ultimately dissolve into the matrix, with large B2 and σ greatly refined and the smaller B2 completely dissolved.
- 3) XRD was used to estimate dislocation density and strengthening analysis was performed on both alloys, with calculated strength closely matching the average hardness from the near edge of the discs. The dominant strengthening mechanism was found to be grain boundary strengthening for both alloys.

6. Acknowledgments

This research was supported by a research grant (award number DMR-2207965) from U.S. National Science Foundation. RZV acknowledges the support in part from Russian Science

Foundation (Grant number 22-19-00445). RKI is grateful to the Russian Science Foundation for supporting project 22-23-00714. Materials Research Center at Missouri University of Science and Technology is acknowledged for providing access to electron microscopy and X-ray diffraction Dr. Eric Bohannan is thanked for his assistance with X-ray diffraction. Characterization using the Talos F200X and JEM 2100F was performed at the Center for Nanoscale Materials at Argonne National Laboratory under user proposal 75825. Work performed at the Center for Nanoscale Materials, a U.S. Department of Energy Office of Science User Facility, was supported by the U.S. DOE, Office of Basic Energy Sciences, under Contract No. DE-AC02-06CH11357.

References:

- [1] Cantor, B., Chang, I., Knight, P., & Vincent, A. (2004). Microstructural development in equiatomic multicomponent alloys. *Materials Science and Engineering: A*, 375-377, 213–218.
- [2] Miracle, D.B., Senkov, O.N. (2017). A critical review of high entropy alloys and related concepts. *Acta Materialia*, 122, 448-511.
- [3] Yeh, J.-W., Chen, S.-K., Lin, S.-J., Gan, J.-Y., Chin, T.-S., Shun, T.-T., ... Chang, S.-Y. (2004). Nanostructured High-Entropy Alloys with Multiple Principal Elements: Novel Alloy Design Concepts and Outcomes. *Advanced Engineering Materials*, *6*(5), 299–303.
- [4] Wang, X.F., Zhang, Y., Qiao, Y., Chen, G.L. (2007). Novel microstructure and properties of multicomponent CoCrCuFeNiTi_x alloys. *Intermetallics*, 15, 357-362.
- [5] Fu, Z., Chen, W., Wen, H., Zhang, D., Chen, Z., Zheng, B., Zhou, Y., Lavernia, E.J. (2016). Microstructure and strengthening mechanisms in an FCC structured single-phase nanocrystalline Co₂₅Ni₂₅Fe₂₅Al_{7.5}Cu_{17.5} high-entropy alloy. *Acta Materialia*, 107, 59-71.
- [6] Chen, J., Zhou, X., Wang, W., Liu, B., Lu, Y., Yang, W., Xu, D., Liu, Y. (2018). A review on fundamentals of high entropy alloys with promising high-temperature properties. *Journal of Alloys and Compounds*, 760, 15-30.
- [7] Bai, X., Fang, W., Chang, R., Yu, H., Zhang, X., Yin, F. (2019). Effects of Al and Ti additions on precipitation behavior and mechanical properties of Co₃₅Cr₂₅Fe_{40-x}Ni_x TRIP high entropy alloys. *Materials Science and Engineering A*, 767, 138403.
- [8] Liu, Y.Y, Chen, Z., Chen, Y.Z., Shi, J.C., Wang, Z.Y., Wang, S., Liu, F. (2019). Effect of Al content on high temperature oxidation of Al_xCoCrCuFeNi high entropy alloys (x=0, 0.5, 1, 1.5, 2). *Vacuum*, 169, 108837.
- [9] Li, T., Swanson, O.J., Frankel, G.S., Gerard, A.Y., Lu, P., Saal, J.E., Scully, J.R. (2019). Localized corrosion behavior of a single-phase non-equimolar high entropy alloy. *Electrochimica Acta*, 306, 71-84.
- [10] He, M.-R., Wang, S., Jin, K., Bei, H., Yasuda, K., Matsumura, S., Higashida, K., Robertson, I.M. (2016). Enhanced damage resistance and novel defect structure of CrFeCoNi under *in situ* electron irradiation. *Scripta Materialia*, 125, 5-9.

- [11] Lu, Y., Huang, H., Gao, X., Ren, C., Gao, J., Zhang, H., Zheng, S., Jin, Q., Zhao, Y., Lu, C., Wang, T., Li, T. (2019). A promising new class of irradiation tolerant materials: Ti₂ZrHfV_{0.5}Mo_{0.2} high-entropy alloy. *Journal of Materials Science and Technology*, 35(3), 369-373.
- [12] Duan, J., He, L., Fu, Z., Hoffman, A., Sridharan, K. & Wen, H. (2021). Microstructure, strength and irradiation response of an ultra-fine grained FeNiCoCr multi-principal element alloy. *Journal of Alloys and Compounds*, 851, 156796.
- [13] Zhang, F., Zhang, C., Chen, S.L., Zhu, J., Cao, W.S., Kattner, U.R. (2014). An understanding of high entropy alloys from phase diagram calculations. *CALPHAD*, 45, 1-10.
- [14] Steurer, W. (2020). Single-phase high-entropy alloys-A critical update. *Materials Characterization*, 162, 110179.
- [15] Otto, F., Dlouhy, A., Somsen, C., Bei, H., Eggeler, G., George, E.P. (2013). The influences of temperature and microstructure on the tensile properties of a CoCrFeMnNi high-entropy alloy. *Acta Materialia*, *61*, 5743-5755.
- [16] He, J.Y., Wang, H., Huang, H.L., Xu, X.D., Chen, M.W., Wu, Y., Liu, X.J., Nieh, T.G., An, K., Lu, Z.P. (2016) A precipitation-hardened high-entropy alloy with outstanding tensile properties. *Acta Materialia*, *102*, 187-196.
- [17] Wang, Q., Ma, Y., Jiang, B., Li, X., Shi, Y., Dong, C., Liaw, P.K. (2016). A cuboidal B2 nanoprecipitation-enhanced body-centered-cubic alloy Al_{0.7}CoCrFe₂Ni with prominent tensile properties. *Scripta Materialia*, 120, 85-89.
- [18] He, J.Y., Wang, H., Wu, Y., Liu, X.J., Mao, H.H., Nieh, T.G., Liu, Z.P. (2016). Precipitation behavior and its effects on tensile properties of FeCoNiCr high-entropy alloys. *Intermetallics*, 79, 41-52.
- [19] Liang, Y.-J., Wang, L., Wen, Y., Cheng, B., Wu, Q., Cao, T., Xiao, Q., Xue, Y., Sha, G., Wang, Y., Ren, Y., Li, X., Wang, L., Wang, F., Cai, H. (2018). High-content ductile coherent nanoprecipitates achieve ultrastrong high-entropy alloys. *Nature Communications*, *9*(1), 4063.
- [20] Zhao, Y.Y., Chen, H.W., Lu, Z.P., Nieh, T.G. (2018). Thermal Stability and coarsening of coherent particles in a precipitation-hardened (NiCoFeCr)₉₄Ti₂Al₄ high-entropy alloy. *Acta Materialia*, 147, 184-194.
- [21] Yeli, G., Chen, D., Yabuuchi, K., Kimura, A., Liu, S., Lin, W., Zhao, Y., Zhao, S., Kai, J.-J. (2020). The stability of γ ' precipitates in a multi-component FeCoNiCrTi_{0.2} alloy under elevated-temperature irradiation, *Journal of Nuclear Materials*, *540*, 152364.
- [22] Ni, S., Wang, Y. B., Liao, X. Z., Alhajeri, S. N., Li, H. Q., Zhao, Y. H., Lavernia, E. J., Ringer, S. P., Langdon, T. G., & Zhu, Y. T. (2011). Grain growth and dislocation density evolution in a nanocrystalline Ni–Fe alloy induced by high-pressure torsion. *Scripta Materialia*, 64(4), 327–330.
- [23] Dong, W., Zhou, Z., Zhang, M., Ma, Y., Yu, P., Liaw, P. K., & Li, G. (2019). Applications of high-pressure technology for high-entropy alloys: A Review. *Metals*, *9*(8), 867.

- [24] An, X. H., Lin, Q. Y., Sha, G., Huang, M. X., Ringer, S. P., Zhu, Y. T., & Liao, X. Z. (2016). Microstructural evolution and phase transformation in twinning-induced plasticity steel induced by high-pressure torsion. *Acta Materialia*, 109, 300–313.
- [25] Scheriau, S., Zhang, Z., Kleber, S., & Pippan, R. (2011). Deformation mechanisms of a modified 316L austenitic steel subjected to high pressure torsion. *Materials Science and Engineering:* A, 528(6), 2776–2786.
- [26] Das, M., Das, G., Ghosh, M., Wegner, M., Rajnikant, V., GhoshChowdhury, S., & Pal, T. K. (2012). Microstructures and mechanical properties of HPT processed 6063 Al alloy. *Materials Science and Engineering: A*, 558, 525–532.
- [27] Tang, Q. H., Huang, Y., Huang, Y. Y., Liao, X. Z., Langdon, T. G., & Dai, P. Q. (2015). Hardening of an Al0.3CoCrFeNi high entropy alloy via high-pressure torsion and thermal annealing. *Materials Letters*, *151*, 126–129.
- [28] Gao, Z., Zhao, Y., Park, J.-M., Jeon, A.-H., Murakami, K., Komazaki, S.-ichi, Tsuchiya, K., Ramamurty, U., & Jang, J.-il. (2022). Decoupling the roles of constituent phases in the strengthening of hydrogenated nanocrystalline dual-phase high-entropy alloys. *Scripta Materialia*, 210, 114472.
- [29] Shahmir, H., Tabachnikova, E., Podolskiy, A., Tikhonovsky, M., & Langdon, T. G. (2018). Effect of carbon content and annealing on structure and hardness of CrFe2NiMnV0.25 highentropy alloys processed by high-pressure torsion. *Journal of Materials Science*, *53*(16), 11813–11822.
- [30] Edalati, P., Mohammadi, A., Tang, Y., Floriano, R., Fuji, M., & Edalati, K. (2021). Phase transformation and microstructure evolution in ultrahard carbon-doped AlTiFeCoNi high-entropy alloy by high-pressure torsion. *Materials Letters*, 302, 130368.
- [31] Yu, P. F., Cheng, H., Zhang, L. J., Zhang, H., Jing, Q., Ma, M. Z., Liaw, P. K., Li, G., & Liu, R. P. (2016). Effects of high pressure torsion on microstructures and properties of an Al0.1CoCrFeNi high-entropy alloy. *Materials Science and Engineering: A*, 655, 283–291.
- [32] Schuh, B., Pippan, R., & Hohenwarter, A. (2019). Tailoring bimodal grain size structures in nanocrystalline compositionally complex alloys to improve ductility. *Materials Science and Engineering: A*, 748, 379–385.
- [33] Lee, D.-H., Seok, M.-Y., Zhao, Y., Choi, I.-C., He, J., Lu, Z., Suh, J.-Y., Ramamurty, U., Kawasaki, M., Langdon, T. G., & Jang, J.-il. (2016). Spherical nanoindentation creep behavior of nanocrystalline and coarse-grained cocrfemnni high-entropy alloys. *Acta Materialia*, 109, 314–322.
- [34] Zhang, Y., Jin, S., Trimby, P. W., Liao, X., Murashkin, M. Y., Valiev, R. Z., Liu, J., Cairney, J. M., Ringer, S. P., & Sha, G. (2019). Dynamic precipitation, segregation and strengthening of an Al-Zn-Mg-cu alloy (AA7075) processed by high-pressure torsion. *Acta Materialia*, 162, 19–32.

- [35] Azzeddine, H., Mehdi, B., Hennet, L., Thiaudière, D., Alili, B., Kawasaki, M., Bradai, D., & Langdon, T. G. (2014). An in situ synchrotron X-ray diffraction study of precipitation kinetics in a severely deformed Cu–Ni–Si Alloy. *Materials Science and Engineering: A*, 597, 288–294.
- [36] Cepeda-Jiménez, C. M., García-Infanta, J. M., Zhilyaev, A. P., Ruano, O. A., & Carreño, F. (2011). Influence of the thermal treatment on the deformation-induced precipitation of a hypoeutectic Al–7 wt% Si casting alloy deformed by high-pressure torsion. *Journal of Alloys and Compounds*, 509(3), 636–643.
- [37] Meng, F., Rosalie, J. M., Singh, A., Somekawa, H., & Tsuchiya, K. (2014). Ultrafine grain formation in Mg–Zn alloy by in situ precipitation during high-pressure torsion. *Scripta Materialia*, 78-79, 57–60.
- [38] Sun, W. T., Qiao, X. G., Zheng, M. Y., He, Y., Hu, N., Xu, C., Gao, N., & Starink, M. J. (2018). Exceptional grain refinement in a Mg alloy during high pressure torsion due to rare earth containing nanosized precipitates. *Materials Science and Engineering: A*, 728, 115–123.
- [39] Straumal, B. B., Kilmametov, A. R., Baretzky, B., Kogtenkova, O. A., Straumal, P. B., Lityńska-Dobrzyńska, L., Chulist, R., Korneva, A., & Zięba, P. (2020). High pressure torsion of Cu–Ag and Cu–Sn Alloys: Limits for solubility and dissolution. *Acta Materialia*, 195, 184–198.
- [40] Straumal, B. B., Pontikis, V., Kilmametov, A. R., Mazilkin, A. A., Dobatkin, S. V., & Baretzky, B. (2017). Competition between precipitation and dissolution in Cu–Ag Alloys under high pressure torsion. *Acta Materialia*, 122, 60–71.
- [41] Liu, X., Ding, H., Huang, Y., Bai, X., Zhang, Q., Zhang, H., Langdon, T. G., & Cui, J. (2021). Evidence for a phase transition in an AlCrFe2Ni2 high entropy alloy processed by high-pressure torsion. *Journal of Alloys and Compounds*, 867, 159063.
- [42] Park, N., Lee, B.-J., & Tsuji, N. (2017). The phase stability of equiatomic CoCrFeMnNi highentropy alloy: Comparison between experiment and calculation results. *Journal of Alloys and Compounds*, 719, 189–193.
- [43] Pommeranke, H., Duan, J., Curtis, N., DeLibera, V., Bratten, A., Hoffman, A., Buchely, M., O'Malley, R., Wen, H. (2023). A strong and ductile cobalt-free solid-solution Fe₃₀Ni₃₀Mn₃₀Cr₁₀ multi-principal element alloy from hot rolling. *Journal of Alloys and Compounds*, 948, 169566.
- [44] Moon, J., Qi, Y., Tabachnikova, E., Estrin, Y., Choi, W.-M., Joo, S.-H., Lee, B.-J., Podolskiy, A., Tikhonovsky, M., & Kim, H. S. (2017). Deformation-induced phase transformation of Co20Cr26Fe20Mn20Ni14 high-entropy alloy during high-pressure torsion at 77 K. *Materials Letters*, 202, 86–88.
- [45] Li, Z., Fu, L., Peng, J., Zheng, H., Ji, H., Sun, Y., Ma, S., Shan, A. (2020). Improving mechanical properties of an FCC high-entropy alloy by γ' and B2 precipitates strengthening, *Materials Characterization*, 159, 109989.
- [46] Zhang, L.J., Guo, K., Tang, H., Zhang, M.D., Fan, J.T., Cui, P., Ma, Y.M., Yu, P.F., Li, G. (2019). The microstructure and mechanical properties of novel Al-Cr-Fe-Mn-Ni high-entropy

- alloys with trimodal distributions of coherent B2 precipitates, *Materials Science and Engineering: A*, 757, 160-171.
- [47] Liu, W.H., Wu, Y., He, J.Y., Nieh, T.G., Lu, Z.P. (2013). Grain growth and the Hall-Petch relationship in a high-entropy FeCrNiCoMn alloy, *Scripta Materialia*, 68, 526-529.
- [48] Wen, H., Topping, T. D., Isheim, D., Seidman, D. N., & Lavernia, E. J. (2013). Strengthening mechanisms in a high-strength bulk nanostructured Cu–Zn–Al alloy processed via cryomilling and spark plasma sintering. *Acta Materialia*, 61(8), 2769–2782.
- [49] Zhao, W., Han, J.-K., Kuzminova, Y. O., Evlashin, S. A., Zhilyaev, A. P., Pesin, A. M., Jang, J.-il, Liss, K.-D., & Kawasaki, M. (2021). Significance of grain refinement on micro-mechanical properties and structures of additively-manufactured CoCrFeNi high-entropy alloy. *Materials Science and Engineering: A*, 807, 140898.
- [50] Duan, J. Q., Quadir, M. Z., & Ferry, M. (2015). An analytical framework for predicting the limit in structural refinement in accumulative roll bonded nickel. *Metallurgical and Materials Transactions A*, 47(1), 471–478.
- [51] Mohamed, F. A., & Dheda, S. S. (2012). On the minimum grain size obtainable by high-pressure torsion. *Materials Science and Engineering: A*, 558, 59–63.
- [52] Sabbaghianrad, S., Torbati-Sarraf, S. A., & Langdon, T. G. (2018). An investigation of the limits of grain refinement after processing by a combination of severe plastic deformation techniques: A comparison of Al and MG Alloys. *Materials Science and Engineering: A*, 712, 373–379.
- [53] Bachmaier, A., Hafok, M., Schuster, R., & Pippan, R. (2010). Limitations in the refinement by severe plastic deformation: the effect of processing. *Rev. Adv. Mater. Sci*, 25, 16-22.
- [54] Hafok, M., & Pippan, R. (2008). Athermal and thermal limits of the grain refinement by SPD. *Materials Science Forum*, *584-586*, 938–943.
- [55] Kuzovchikov, S., Bajenova, I., Khvan, A., & Cheverikin, V. (2023). Investigation of the hardness and enthalpy of formation of the Sigma phase and the phase equilibria in the Cr-Co-Mn system. *Journal of Alloys and Compounds*, 964, 171263.
- [56] Dey, G. K., & Sekhar, J. A. (1997). Micropyretic synthesis of tough NiAl alloys. *Metallurgical and Materials Transactions B*, 28(5), 905-918.
- [57] Ivanisenko, Y., Lojkowski, W., Valiev, R.Z., Fecht, H.-J. (2003). The mechanism of formation of nanostructure and dissolution of cementite in a pearlitic steel during high pressure torsion. *Acta Materialia*, *51*, 5555-5570.
- [58] Korneva, A., Straumal, B., Kilmametov, A., Chulist, R., Cios, G., Baretzky, B., Zieba, P. (2019). Dissolution of Ag precipitates in the Cu-8 at% Ag alloy deformed by high pressure torsion. *Materials*, *12*, 447-459.

- [59] Beach, J.A., Wang, M., Bellon, P., Dillon, S., Ivanisenko, Y., Boll, T., Averbeck, R.S. (2017). Self-organized, size-selection of precipitates during severe plastic deformation of dilute Cu-Nb alloys at low temperatures. *Acta Materialia*, *140*, 217-223.
- [60] Languillaume, J., Kapelski, G., Baudelet, B. (1997). Cementite dissolution in heavily cold drawn pearlitic steel wires. *Acta Metallurgica*, 45(3), 1201-1212.
- [61] Jacob, K., Roy, A., Gururajan, M.P., Nagamani Jaya, B. (2022). Effect of dislocation network on precipitate morphology and deformation behaviour in maraging steels: Modelling and experimental validation. *Materialia*, 21, 101358.

Figures

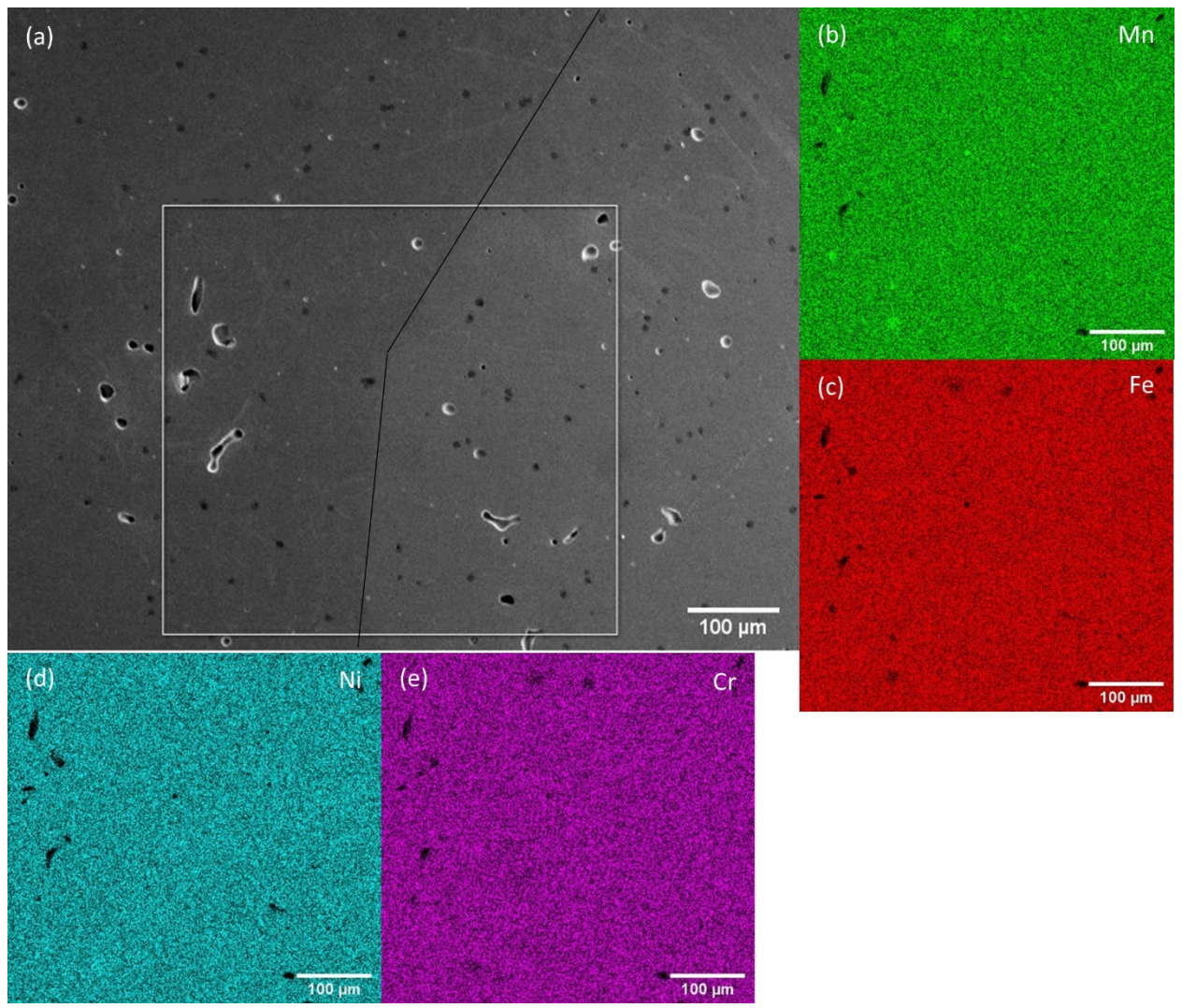


Figure 1: FeNiMnCr alloy after casting and homogenization, before HPT. (a) SEM image, and EDS elemental maps of (b) Mn, (c) Fe, (d) Ni, (e) Cr. The microstructure is mostly homogeneous, except for Mn inclusions. The grain boundary has been marked for clarity.

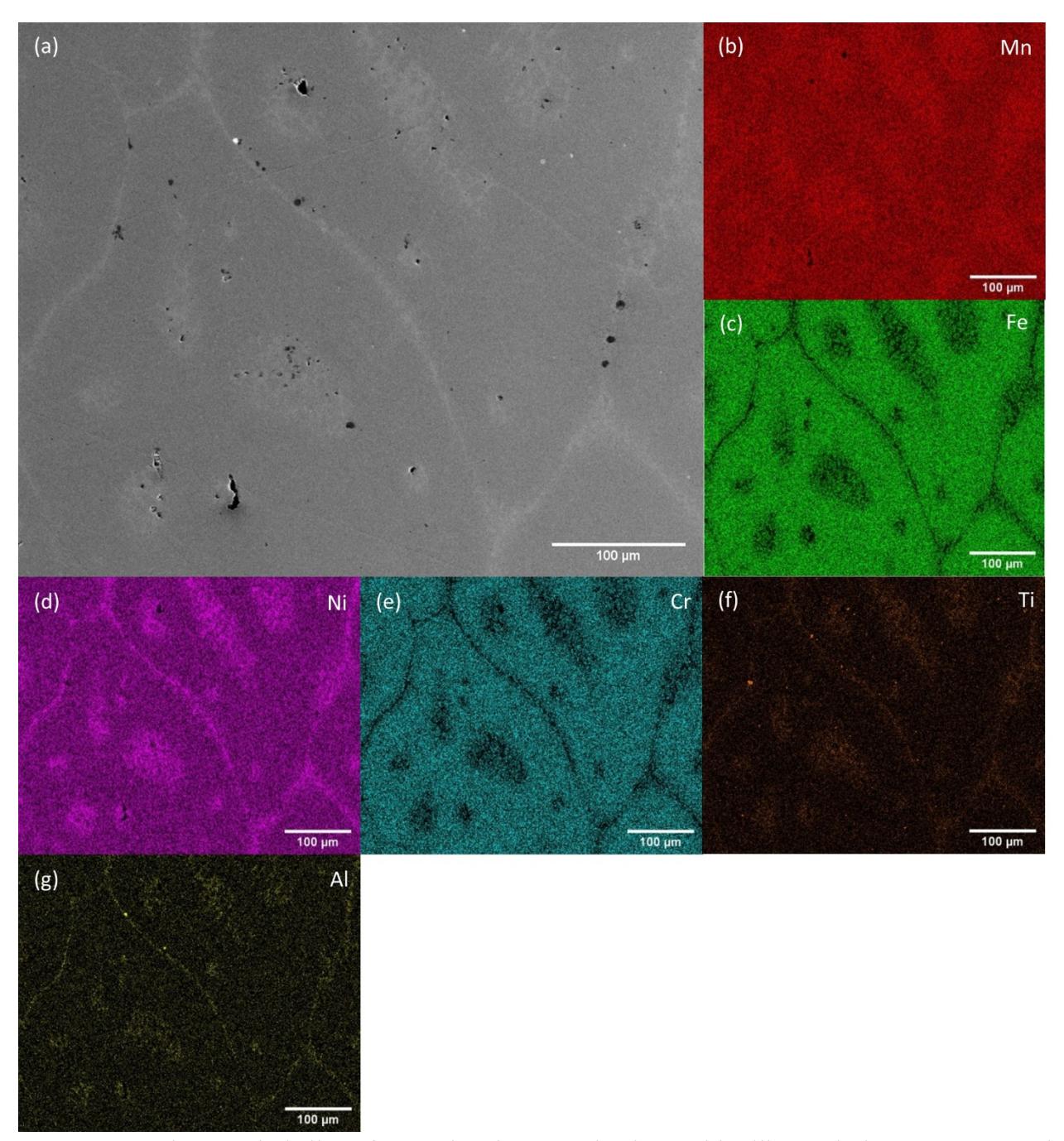


Figure 2: FeNiMnCrTiAl alloy after casting, homogenization, cold rolling, solution treatment, and aging at 800 °C for 18 hours, before HPT. (a) SEM image, with EDS elemental maps of (b) Mn, (c) Ni, (d) Fe, (e) Cr, (f) Ti, (g) Al. Note the segregations of Ni, Ti, and Al on grain boundaries and enrichment inside grains.

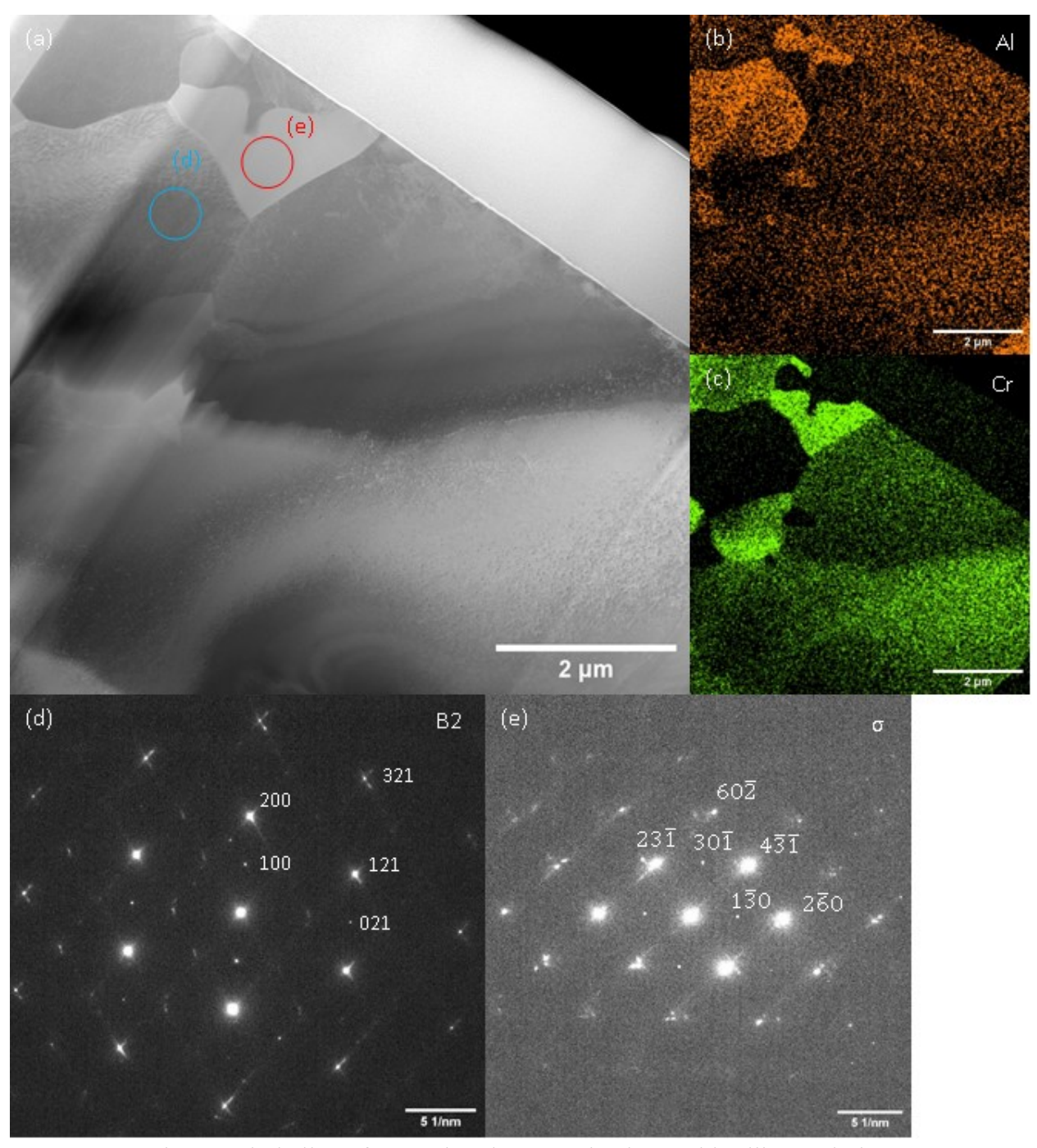


Figure 3: FeNiMnCrTiAl alloy after casting, homogenization, cold rolling, solution treatment, and aging at 800 °C for 18 hours, before HPT. (a) STEM-HAADF image, with EDS elemental maps of (b) Al and (c) Cr. Areas of Al and Cr enrichment were identified, and diffraction patterns were indexed as B2 and σ in (d) and (e), respectively.

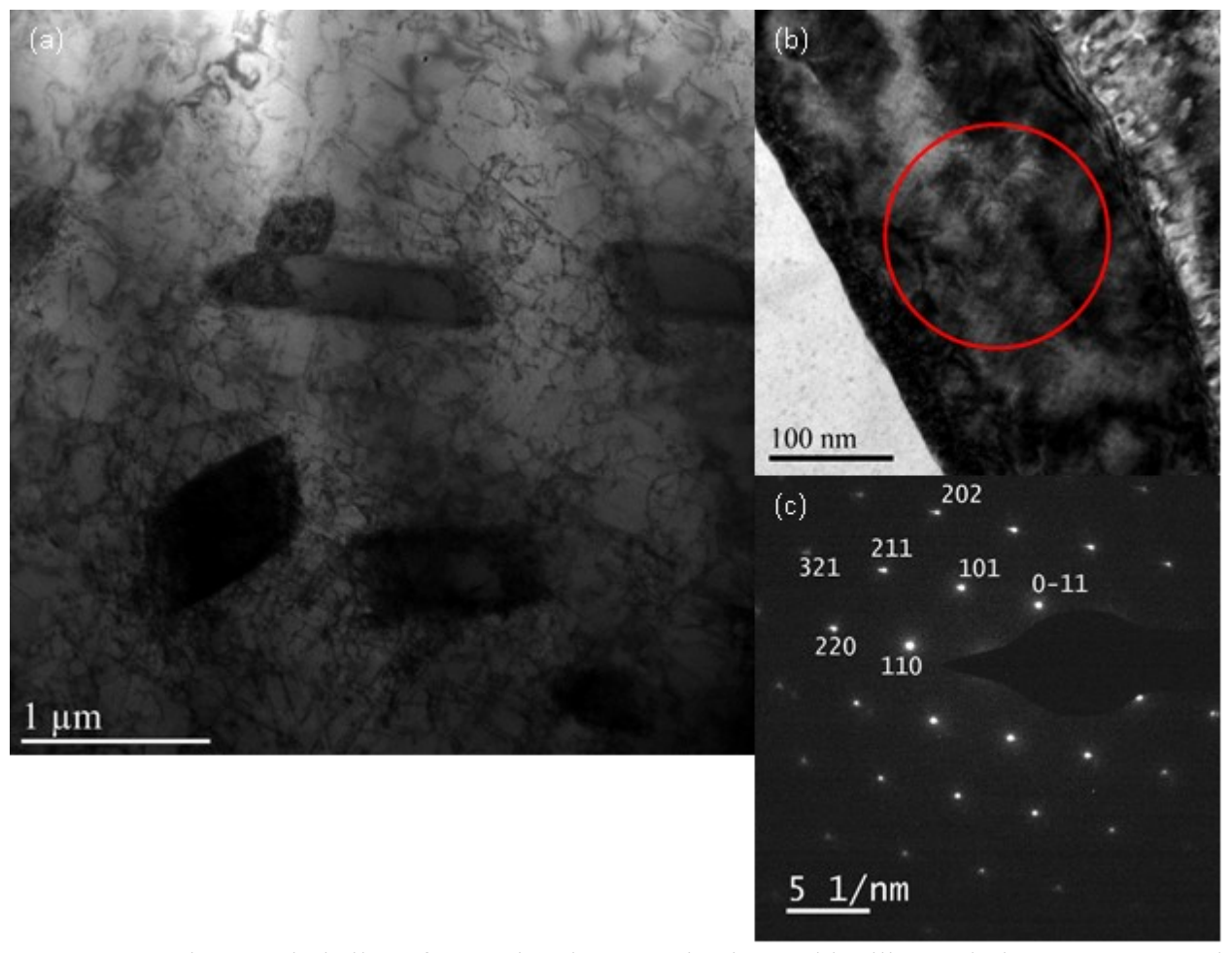


Figure 4: FeNiMnCrTiAl alloy after casting, homogenization, cold rolling, solution treatment, and aging at 800 °C for 18 h, before HPT. (a) TEM image of B2 precipitates, showing typical morphology, (b) TEM image of a B2 precipitate with a selected area circled, (c) SAED of circled area, indexed as B2 along the [111] zone axis.

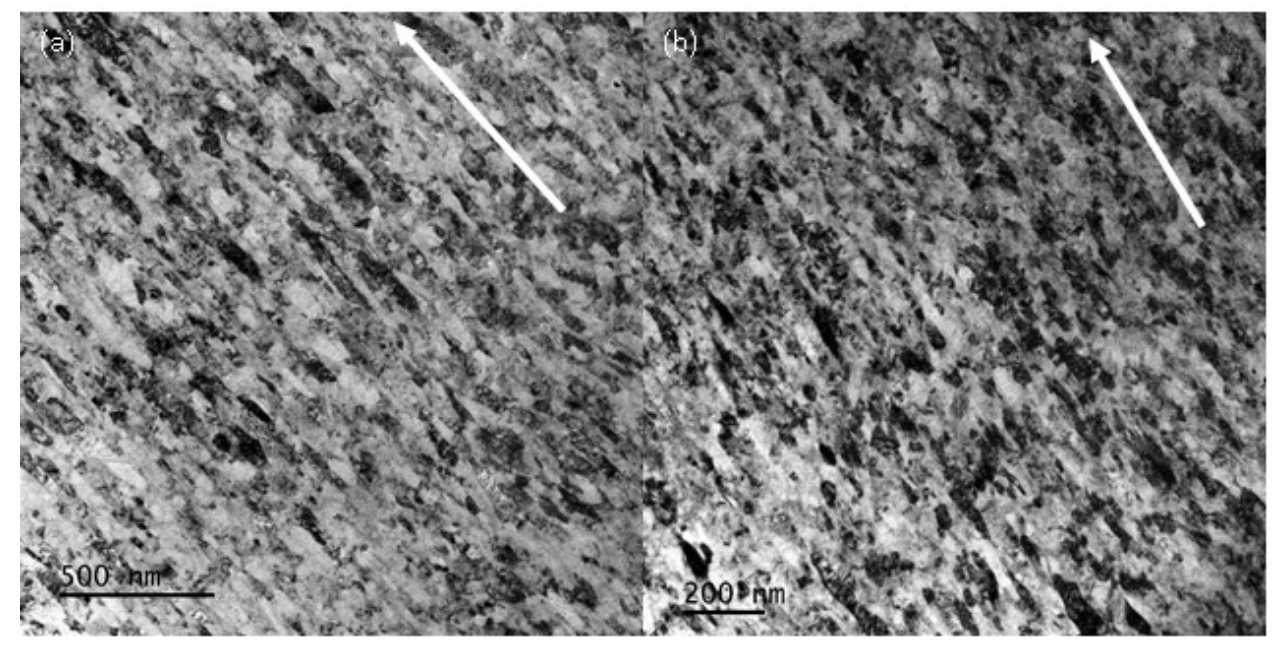


Figure 5: TEM images of the microstructure after HPT processing in (a) FeNiMnCr and (b) FeNiMnCrTiAl. Note the direction (white arrow) along which grains are elongated. Both images were taken at 4 mm distance from the center of the HPT disc.

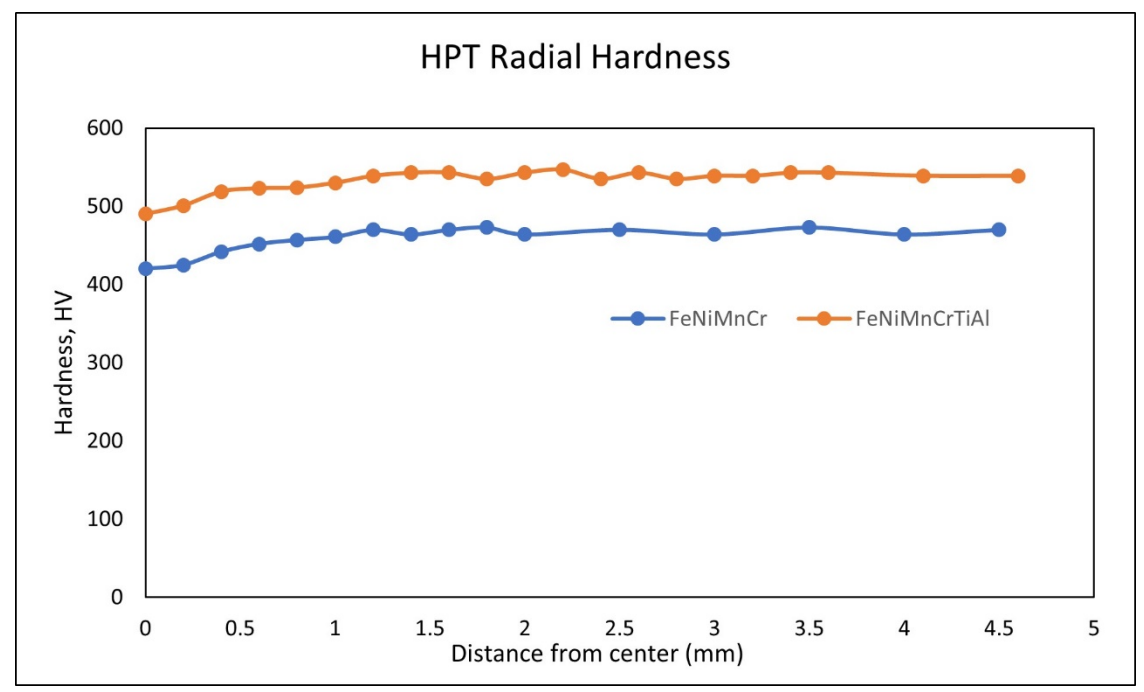


Figure 6: Vickers hardness as a function of radial distance for HPT processed HEAs. Hardness increases slightly along the radial direction. FeNiMnCrTiAl has consistently higher hardness than FeNiMnCr.

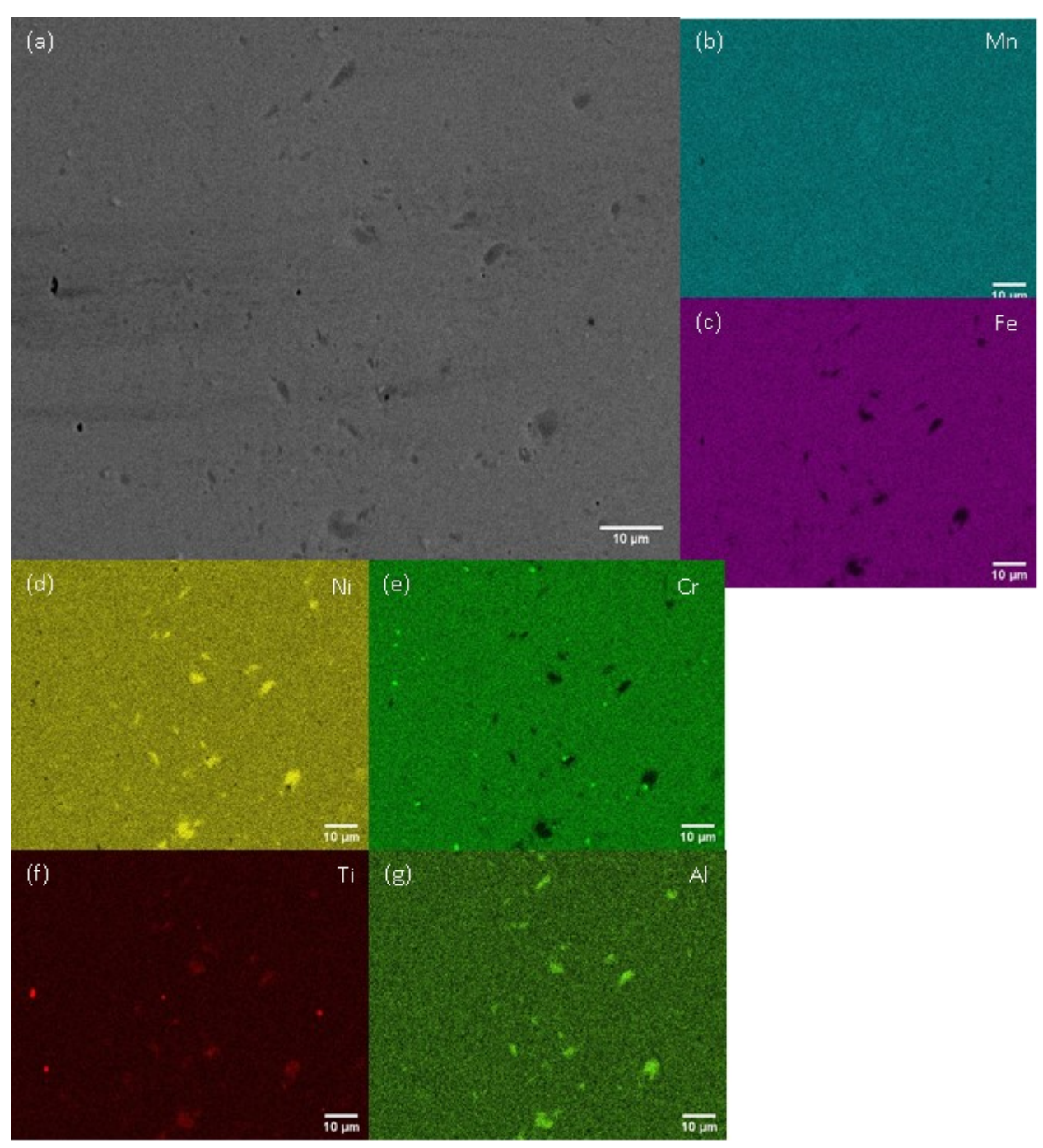


Figure 7: Microscale microstructure and elemental distribution in FeNiMnCrTiAl alloy after HPT processing to show precipitates at distance of 4 mm from center (same general area as TEM specimens in Figures 4 and 8): (a) SEM image, and EDS elemental maps of (b) Mn, (c) Fe, (d) Ni, (e) Cr, (f) Ti, (g) Al. Note areas of Ni, Al and Ti enrichments. Cr enriched spots are likely retained σ , but they are very sparse (0.27% of area).

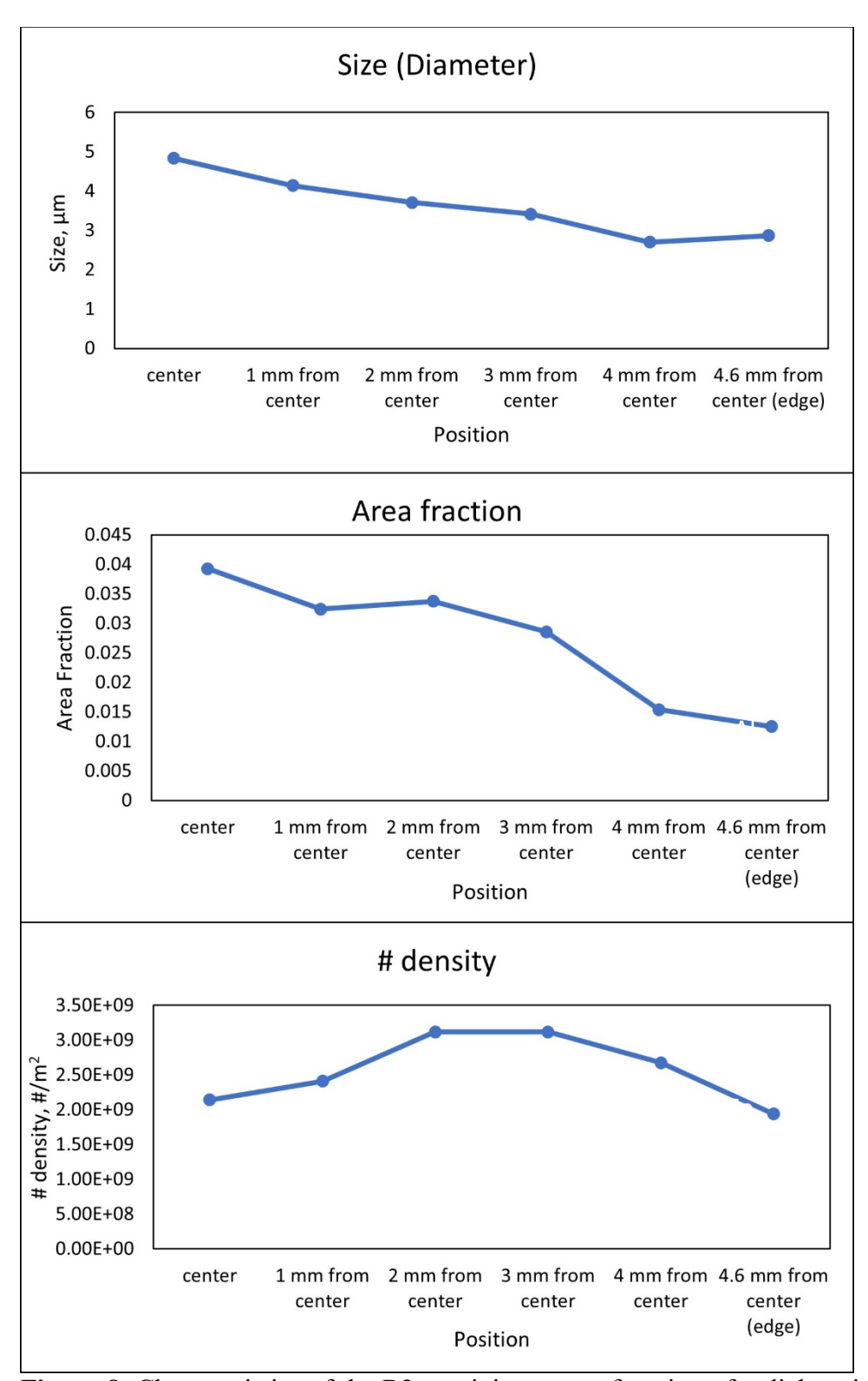


Figure 8: Characteristics of the B2 precipitates as a function of radial position: (a) size, (b) area fraction, (c) number density. Note the decreasing size trend, as well as initial increase and then decrease in number density.

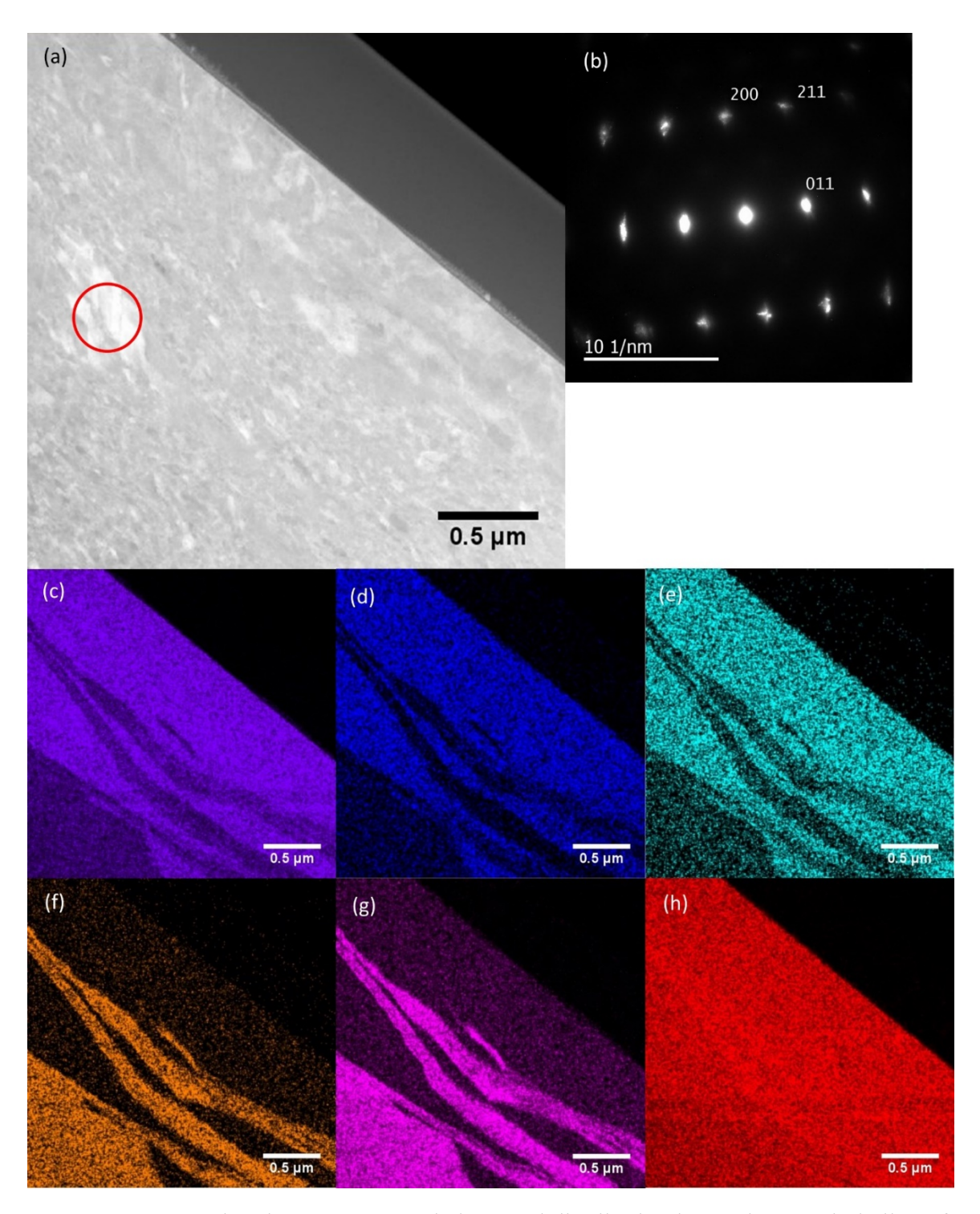


Figure 9: Nanoscale microstructure and elemental distribution in FeNiMnCrTiAl alloy after HPT processing (TEM sample was taken directly from one of the NiTiAl enriched areas visible in Figure 7): (a) STEM image; (b) SAED pattern taken from the marked area in (a), which was indexed as BCC (B2) structure. EDS elemental maps of (c) Ni, (d) Al, (e) Ti, (f) Cr, (g) Fe, and (h) Mn show enrichment of Ni, Al, and Ti in the region selected in (a), indicating that the region is B2.

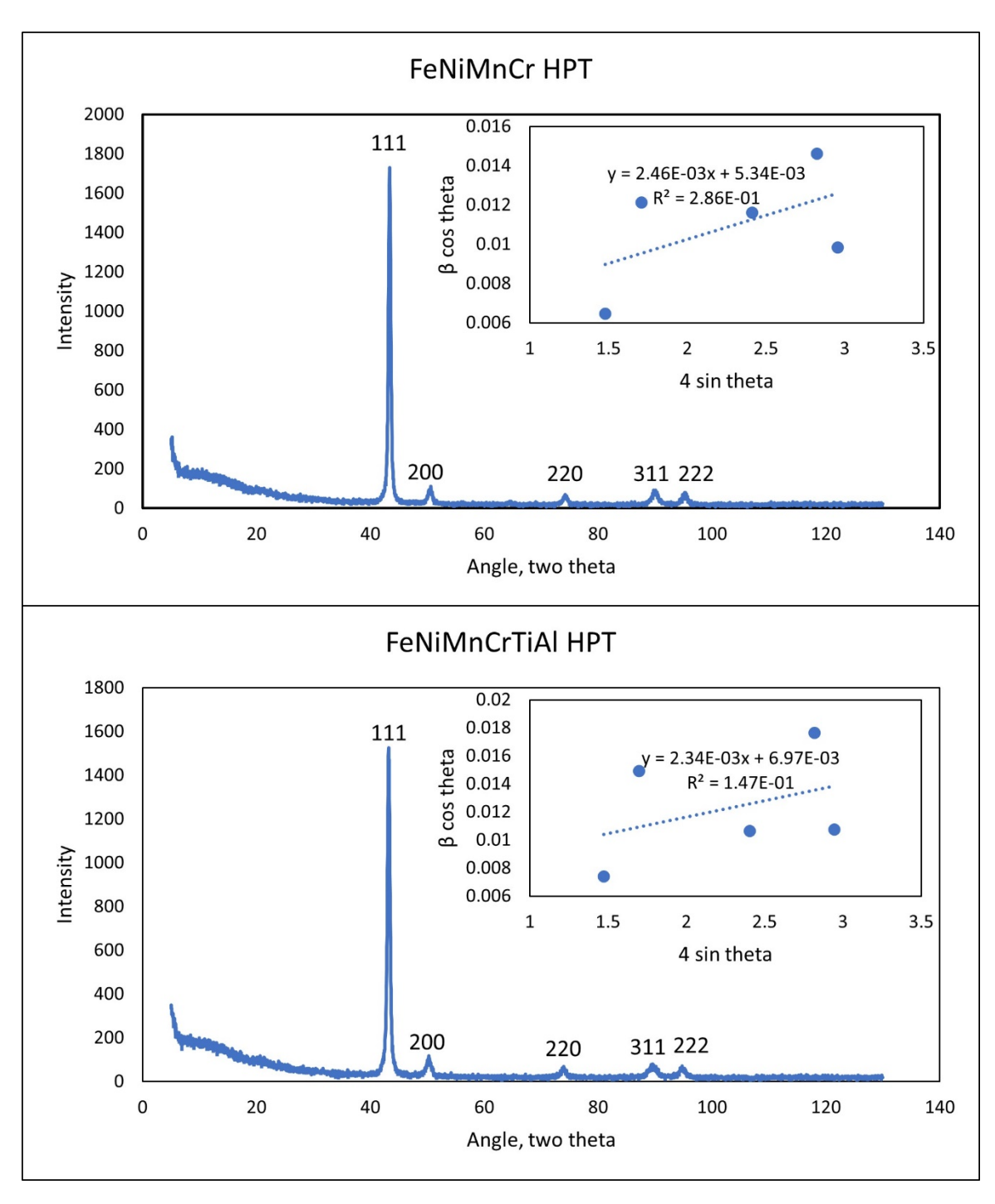


Figure 10: XRD patterns of HPT discs used to estimate dislocation density: (a) FeNiMnCr, (b) FeNiMnCrTiAl. Williamson-Hall plots are included as insets. All peaks belong to FCC and are marked on the patterns.

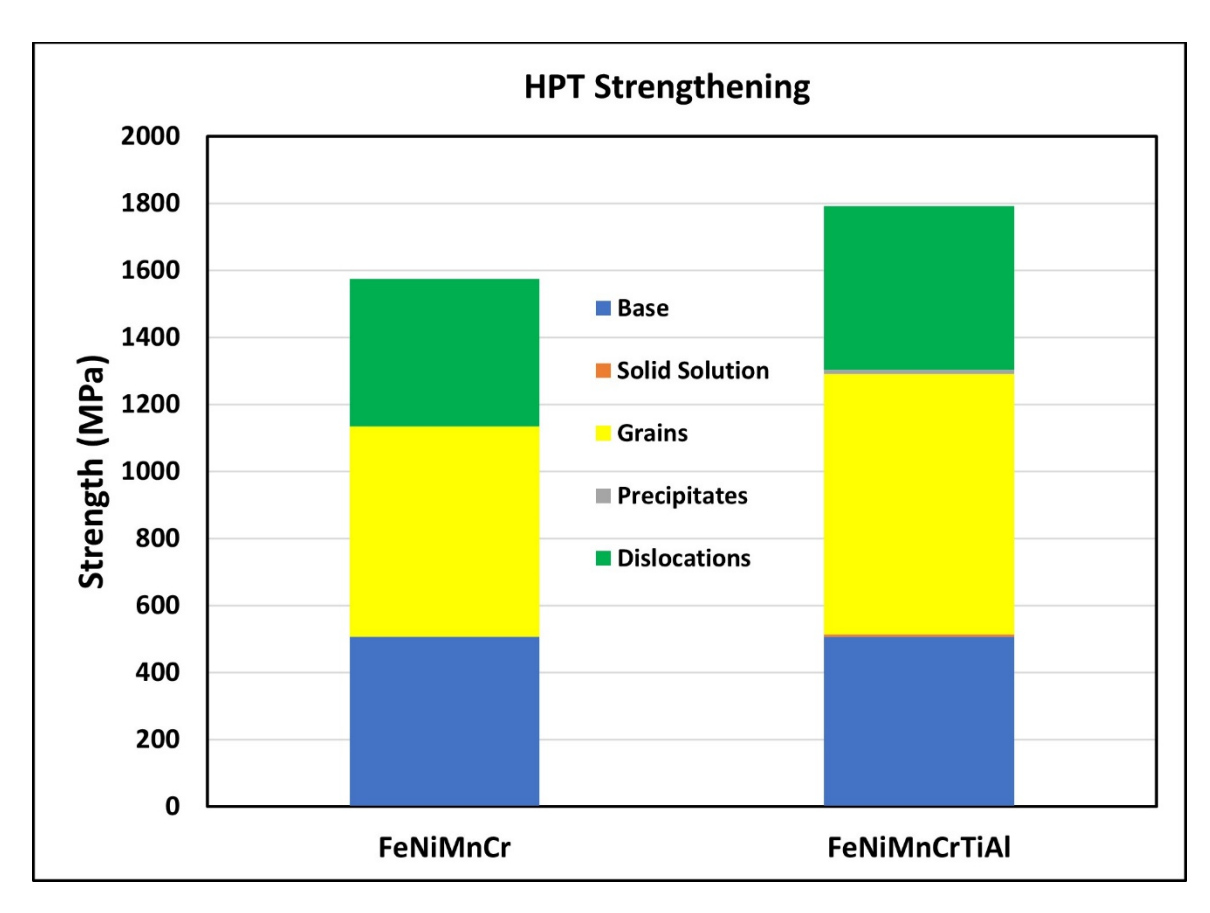


Figure 11: Strengthening analysis for HPT-processed HEAs, indicating strengthening contributions from different strengthening mechanisms. Left is the FeNiMnCr alloy, right is the FeNiMnCrTiAl.